Grain refining mechanisms in Mg–Al alloys with Al_4C_3 microparticles

Sunya Nimityongskul [a], Milton Jones [a], Hongseok Choi [a], Roderic Lakes [b], Sindo Kou [c], Xiaochun Li [a,*]

[a] Department of Mechanical Engineering, University of Wisconsin-Madison, 1513 University Avenue, Madison, WI 53706, United States
[b] Department of Engineering Physics, University of Wisconsin-Madison, WI 53706, United States
[c] Department of Materials Science and Engineering, University of Wisconsin-Madison, WI 53706, United States

ARTICLE INFO

ABSTRACT

Experiments were conducted to examine the grain refining mechanisms in AM60B, pure Mg, and Mg–6%Al with the addition of 5 wt% aluminum carbide (Al_4C_3). Grain refinement was observed in the AM60B and pure Mg with the addition of 5 wt% Al_4C_3 via two different mechanisms respectively, i.e. duplex nucleation hypothesis ($Al_4C_3 \rightarrow Al_8Mn_5 \rightarrow \alpha$-Mg) in AM60B and Al_4C_3 nuclei hypothesis ($Al_4C_3 \rightarrow \alpha$-Mg) in pure Mg. It is suggested that Mn is required to facilitate significant grain refinement in Mg–Al alloys containing $\geq 6\%$ Al due to the segregating behavior of Al_4C_3 particles to the solid–liquid (S–L) interface. Mechanical properties (yield strength, tensile strength, ductility, and microhardness) were enhanced by the addition of Al_4C_3 to AM60B alloy.

1. Introduction

Magnesium alloys are becoming ever more prevalent in automotive and aerospace industries as energy conservation and performance demands increase. Mg alloys being one-third lighter than the equal volume of aluminum alloys is one of the contributing factors that makes these alloys so desirable [1]. The desirable low density of Mg alloys is often outweighed by the poor mechanical performance exhibited at elevated temperatures making aluminum alloys a more attractive option [1–4]. Various magnesium alloy grain refining technologies lend way to increased mechanical properties with negligible changes in density and further understanding of the underlying refinement mechanisms could results in more effective refinement.

There are a variety of different methods to achieve refined equiaxed grains in Mg alloys: rapid cooling, melt super heating, alloying addition of Zr and carbon inoculation. Rapid cooling may not be a viable option for particular castings, and super heating uses extra energy and increases oxidation of the melt [3]. Using the alloying addition of Zr with Mg–Al alloys will poison the alloy due to the formation of stable Al–Zr intermetallics [2,3]. Carbon inoculation utilizing C_2Cl_6 can provide significant refinement in Mg–Al alloys; however, toxic chlorine gas is released during the process creating a hazardous work environment [5,13]. The most commonly accepted theory of carbon inoculation based refinement in Mg–Al alloy systems is that carbon reacts with Al in the melt creating aluminum carbide (Al_4C_3) particles (stable to 2200 °C) which promote grain refinement [3,5–11]. It has been hypothesized that carbon reacts with Al to form Al_2CO [12,14]; however it has been found to be thermodynamically improbable to form Al–C–O compounds with extremely low partial pressures of oxygen in the Mg–Al melt [6,7].

The most commonly accepted hypothesized mechanism by which Al_4C_3 refines Mg alloys is that the α-Mg is nucleated at the surface of the Al_4C_3 particles [6–12,14]. Kim et al. propose a theory of duplex nucleation based grain refinement which states that the surface of Al_4C_3 nucleates polygonal Al_8Mn_5, which in turn provides a nucleating surface for α-Mg yielding significant grain refinement in Mn-containing Mg–Al alloy systems ($Al_4C_3 \rightarrow Al_8Mn_5 \rightarrow \alpha$-Mg) [5]. Kim et al. find if the commonly accepted theory of Al_4C_3 ($R\bar{3}m$, $a = 3.335$ Å, $c = 24.967$ Å) nucleating α-Mg ($P6_3$/mmc, $a = 3.209$ Å, $c = 5.211$ Å) based on lattice parameters can be supported, then Al_8Mn_5 ($R3m$, $a = 12.64$ Å, $c = 15.855$ Å) can also be nucleated from Al_4C_3 based on these same crystallographic parameters [5]. Some investigations have been conducted only using high purity Mg–Al alloys free of Mn [6–8]; however commercial Mg alloys have Mn added to the alloy to control the iron content [2,3]. The addition of Mn to Mg alloys is also used to control corrosion behavior and added when good ductility and impact strength are desired [9]. It is important to study the underlying mechanisms for carbon inoculation based grain refinement in commercial alloys because high purity contaminant free Mg–Al alloys are not an economically viable option for industry. The objective of this investigation is to evaluate enhancements in mechanical properties of AM60B/5 wt%Al_4C_3 at elevated temperatures, and investigate the grain refining mechanisms related to the addition of Al4C3 to AM60B, Mg, and Mg–6%Al.

* Corresponding author. Tel.: +1 608 2626142; fax: +1 608 2652316.
E-mail address: xcli@engr.wisc.edu (X. Li).

2. Experimental procedure

Fig. 1 illustrates the experimental setup schematic of ultrasonic cavitation based solidification processing of micro-sized Al_4C_3 in an AM60B matrix. The size of the Al_4C_3 microparticles used was <44 μm. The nominal alloy composition of AM60B is 5.5–6.5% Al, 0.25% Mn min, 0.10% Si max, 0.22% Zn max, 0.005% Fe max, 0.010% Cu max, 0.002% Ni max, max total 0.003% other, and the remaining balance Mg [15]. The experimental system was comprised of resistance heating furnace for melting the magnesium alloy, microparticle feeding mechanism, protective gas system, and an ultrasonic processing unit. The crucible used for melting and ultrasonic processing is made of mild steel with an inside diameter of 114 mm and a height of 127 mm. A Permendur power ultrasonic probe made of niobium C-103 was used to generate a 17.5 kHz and maximum 4.0 kW power output (Advanced Sonics, LLC, Oxford, CT) for melt processing. The niobium C-103 probe was 31.12 mm (1.225 in.) in diameter and 223.5 mm (8.8 in.) in length. The ultrasonic probe was dipped into the melt about 13 mm. A thin walled niobium cage (31.8 mm top diameter, 88.9 mm base diameter; 76.2 mm high) in a shape of truncated cone was used to hold microparticles inside the melt pool during the ultrasonic processing. The niobium cage has a total of 55 holes 7.94 mm in diameter to allow the circulation of the melt and microparticles.

Approximately 800 g AM60B was melted in the steel crucible while being protected by CO_2 + 0.75% SF6. Once the melt temperature of 725 °C was attained the niobium cage containing 5 wt% Al_4C_3 microparticles was submerged beneath the ultrasonic probe. The size of the Al_4C_3 microparticles used was <44 μm. The melt was then ultrasonically processed at 3.5 kW power level for 15 min for the samples with and without Al_4C_3 microparticles. The ultrasonic probe and niobium cage were then removed from the melt and the melt was elevated to a pouring temperature of 740 °C. The melt was cast into a steel permanent mold purged with CO_2 + 0.75% SF6 and preheated to 400 °C, which is designed and fabricated according to ASTM B 108-03a. The casting was allowed to cool for 30 min before the mold is opened and the casting is removed. Each casting yielded two standard tensile specimens with a 44.5 mm gage length and 9.5 mm diameter. A graphite pouring cup was used to guide the melt into the mold providing additional head, and also mounted
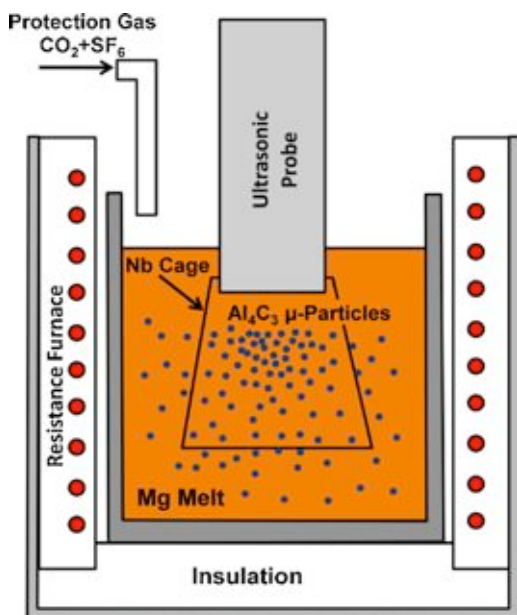
a Pyrotech SIVEX ceramic foam filter (55 mm × 55 mm × 12 mm, 20 pores/in.).

Smaller samples of Mg and Mg–6%Al were processed with and without the addition of Al_4C_3 for microscopic examination (no mechanical testing was performed). Specimens of Mg and Mg–6%Al were processed using a Sonicator 3000 (Misonix Inc.) with a niobium C-103 ultrasonic probe 12.7 mm (.5 in.) in diameter and 92.4 mm (3.64 in.) in length. The ultrasonic probe was dipped into the melt about 6.5 mm. The Mg and Mg–6%Al specimens were made from high purity Mg and Al ingots. Approximately 160 g of Mg or Mg–6%Al was melted in a graphite crucible (1.5 in. diameter, 3 in. height) while being protected by CO_2 + 0.75% SF6. Once the melt temperature of 725 °C was attained, 5 wt%. Al_4C_3 microparticles were manually stirred into the melt and then ultrasonically processed. The melt was then ultrasonically processed at a displacement setting of 6 (60 μm amplitude peak to peak) on the control knob for 15 min without the use of a niobium cage. The ultrasonic probe was then removed from the melt and the melt was elevated to a pouring temperature of 740 °C. The melt was cast into a steel permanent mold purged with CO_2 + 0.75% SF6 and preheated to 400 °C. Each casting yielded two specimens 25 mm long × 25 mm wide × 6.5 mm thick. The specimens were allowed to cool for 30 min then the mold was opened and the castings were removed.

The tensile specimens were tested in a Sintech 10/GL test frame using an extensometer with a 1.0 in. (25.4 mm) gage length clamped to each specimen. The cross head velocity was set to 5 mm/min and the test was run until the strain reached 1%. The test was paused to remove the extensometer, and then resumed with a 5 mm/min cross head velocity until failure. Data was taken from the extensometer until strain reaches 1%, and for strain beyond 1% data was read from the tensile test machine. Tests were also conducted at 125 °C (257 F) and 177° (350 F). The microstructures of the samples were studied by optical microscopy and scanning electron microscopy (SEM). The samples were cut, mounted, and manually ground and polished. Dry polishing was used when it was needed to reveal the microstructure of Al_4C_3 microparticles in Mg matrix. SEM was done in a LEO 1530 machine. Microhardness tests were conducted with a Buehler Micromet 2003 microhardness tester (load 500 gf, load time 30 s). X-ray diffraction (XRD) analysis was conducted using a Scintag PADV X-ray Diffractometer. Wavelength dispersive spectroscopy (WDS) was performed via electron probe microanalysis (EPMA) on a Cameca SX51.

3. Results and discussion

3.1. Tensile data

Table 1 shows the average yield strength, tensile strength, and ductility of the specimens tested at room temperature, 125 °C (257 F), and 177 °C (350 F). At room temperature, the yield strength of AM60B and AM60B/5%Al_4C_3 is 71 and 89 MPa, respectively. At room temperature the yield strength, tensile strength, and ductility are enhanced by 26%, 11%, and 12%, respectively. At 125 °C the yield strength of AM60B and AM60B/5%Al_4C_3 is 67 and 86 MPa, respectively. At 125 °C the yield strength, tensile strength, and ductility are enhanced by 28%, 10%, and 26%, respectively. At 177 °C the yield strength of AM60B and AM60B/5%Al_4C_3 is 62 and 69 MPa, respectively. At 177 °C the yield strength, tensile strength, and ductility are enhanced by 11%, 4%, and 28%, respectively. It is predicted that the Al_4C_3 microparticles will not soften at elevated temperatures, even up to temperatures melting the AM60B matrix [6]. To further evaluate the AM60B/5%Al_4C_3 high temperature performance a creep test should be completed to compare the pure AM60B and AM60B/5%Al_4C_3. The performance increases seen at all temperatures can be largely attributed to the grain refinement of the AM60B/5%Al_4C_3.

Fig. 1. Schematic of experimental setup for fabricating microcomposites.

Table 1
Pure AM60B and AM60B/5%Al$_4$C$_3$ tested properties at 25 °C, 125 °C, and 177 °C.

Temperature	Yield strength [MPa]	Tensile strength [MPa]	Ductility [%]	Microhardness [HK]	Avg. grain size [μm]
Room temp. 25 °C (72 F)					
Pure AM60B	71	197	8.4	46.4 ± 4.2	254 ± 142
AM60B-5Al$_4$C$_3$	89	218	9.4	57.1 ± 2.6	60 ± 14
Enhancement	26%	11%	12%	23%	–
125 °C (257 F)					
Pure AM60B	67	185	8.6	52.7 ± 1.4	230 ± 124
AM60B-5Al$_4$C$_3$	86	202	10.9	57.5 ± 5.6	51 ± 13
Enhancement	28%	10%	26%	9%	–
177 °C (350 F)					
Pure AM60B	62	144	11.3	54 ± 4.3	240 ± 145
AM60B-5Al$_4$C$_3$	69	150	14.5	63.8 ± 2.7	53 ± 18
Enhancement	11%	4%	28%	18%	–

3.2. Microhardness

Table 1 shows the average microhardness of the specimens tested at room temperature, 125 °C (257 F), and 177 °C (350 F). At room temperature the average microhardness of AM60B and AM60B/5%Al$_4$C$_3$ is 46.4 and 57.1 HK, respectively. The microhardness enhancements in AM60B/5%Al$_4$C$_3$ at room temperature, 125 °C (257 F), and 177 °C (350 F) are 23%, 9%, and 18%, respectively. Microhardness of 125 °C and 177 °C specimens were taken after mechanical testing and conducted at room temperature. The performance increases in microhardness seen at all temperatures can be largely attributed to the grain refinement of the AM60B/5%Al$_4$C$_3$.

3.3. Grain size

Table 1 shows average grain size of the specimens tested at room temperature, 125 °C (257 F) and 177 °C (350 F). Average grain size was measured using the linear intercept method from optical micrographs. The average grain size for AM60B at all temperatures is about 240 μm, and the average grain size for AM60B/5%Al$_4$C$_3$ is about 55 μm (Fig. 2).

3.4. Microstructure

Examination of the AM60B/5%Al$_4$C$_3$ after elevated temperature testing (125 °C, 177 °C) revealed that the intergranular Mg$_{17}$Al$_{12}$ transitions from a massive state (Fig. 3a) to a lamellar state as seen in Fig. 3b. After elevated temperature testing intragranular Mg$_{17}$Al$_{12}$ intermetallic only exists in the massive state <3 μm in size in the AM60B/5%Al$_4$C$_3$. After elevated temperature testing the AM60B specimens contain both massive and lamellar forms of the Mg$_{17}$Al$_{12}$ intermetallic.

In AM60B the Al–Mn intermetallic predominantly forms irregular bar and needle shapes up to 30 μm in length (Fig. 4a). XRD
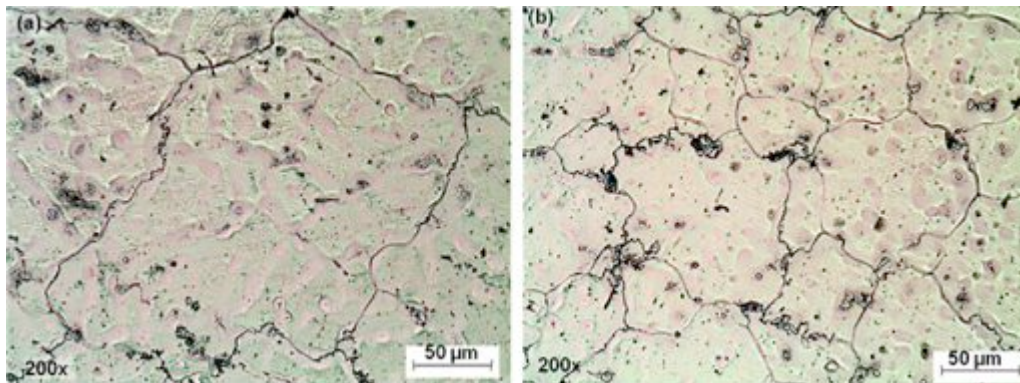
Fig. 2. Optical micrograph of AM60B 25 °C (a) without and (b) with 5 wt% Al$_4$C$_3$.
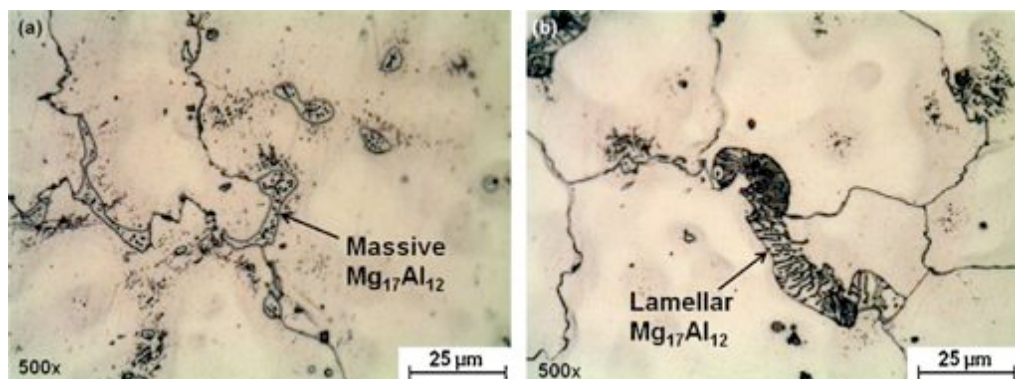
Fig. 3. Optical micrograph of AM60B after testing at 125 °C (a) without and (b) with 5 wt% Al$_4$C$_3$. Figure illustrates the transition of Mg$_{17}$Al$_{12}$ intermetallic from massive to lamellar in AM60B with the addition of Al$_4$C$_3$.
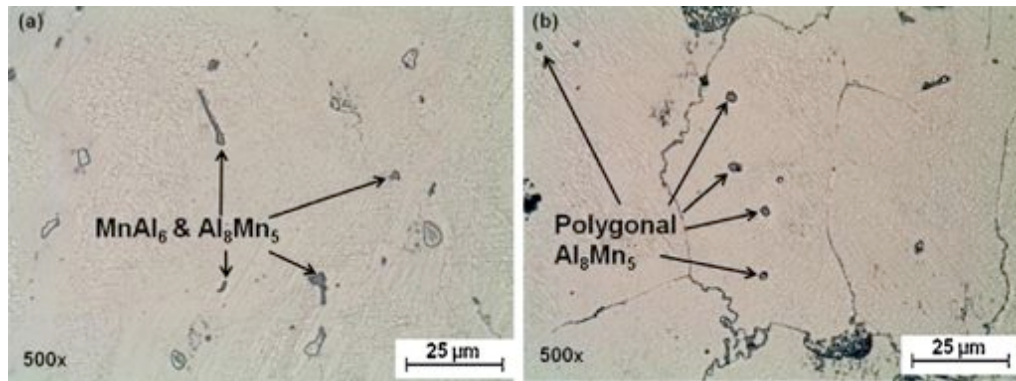
Fig. 4. Optical micrograph of AM60B after testing at 125 °C (a) without and (b) with 5 wt% Al_4C_3, illustrating the transition of Al_8Mn_5 intermetallic from irregular shapes to polygonal form with the addition of 5% Al_4C_3.

analysis indicates that the Al–Mn intermetallic in AM60B is comprised of $MnAl_6$ and Al_8Mn_5. Kim et al. have shown that 0.6 wt%. C_2Cl_6 carbon addition to AZ91 alloys transition the Al–Mn compound from irregular needle shapes to polygonal shapes [5]. Kim et al. analysis of the diffraction pattern identifies the polygonal structures as $Al_8(Mn, Fe)_5$. In AM60B/5%Al_4C_3 the Al–Mn intermetallic only forms polygonal shapes 1–3 μm in size (Fig. 4b). XRD analysis indicates that the polygonal Al–Mn intermetallic in AM60B/5%Al_4C_3 is comprised of Al_8Mn_5. Kim et al. proposed that the C_2Cl_6 reacts with the aluminum in the AZ91 to form Al_4C_3 which acts as a nucleation site for the polygonal Al_8Mn_5 phases. Then the surface of the polygonal Al_8Mn_5 phases nucleates α-Mg yielding significant grain refinement [5]. Therefore if C_2Cl_6 or Al_4C_3 is added to Mn-free Mg–Al alloys there should be no significant grain refinement.

3.5. SEM

From the SEM micrographs and energy dispersive X-ray spectroscopy (EDS) it is confirmed that the irregular bar and needle shapes found in AM60B are comprised of Al–Mn (Fig. 5), and that $Mg_{17}Al_{12}$ exists in both massive and lamellar states. Fig. 6 shows AM60B/5%Al_4C_3 and the Al_8Mn_5 phase nucleated at the surface of an Al_4C_3 particle, within an α-Mg grain. EDS spectral imaging show high concentrations of aluminum and carbon accompanied by a deficiency of magnesium and manganese at the location of the Al_4C_3 (Fig. 6). This further supports the nucleation theory of Al_4C_3 surfaces acting as nucleation sites for the polygonal Al_8Mn_5 phases proposed by Kim et al. Al_4C_3 was not located at grain boundaries, in $Mg_{17}Al_{12}$ phase, or within α-Mg grains, supporting the duplex nucleation theory that the Al_4C_3 is encapsulated within the Al_8Mn_5
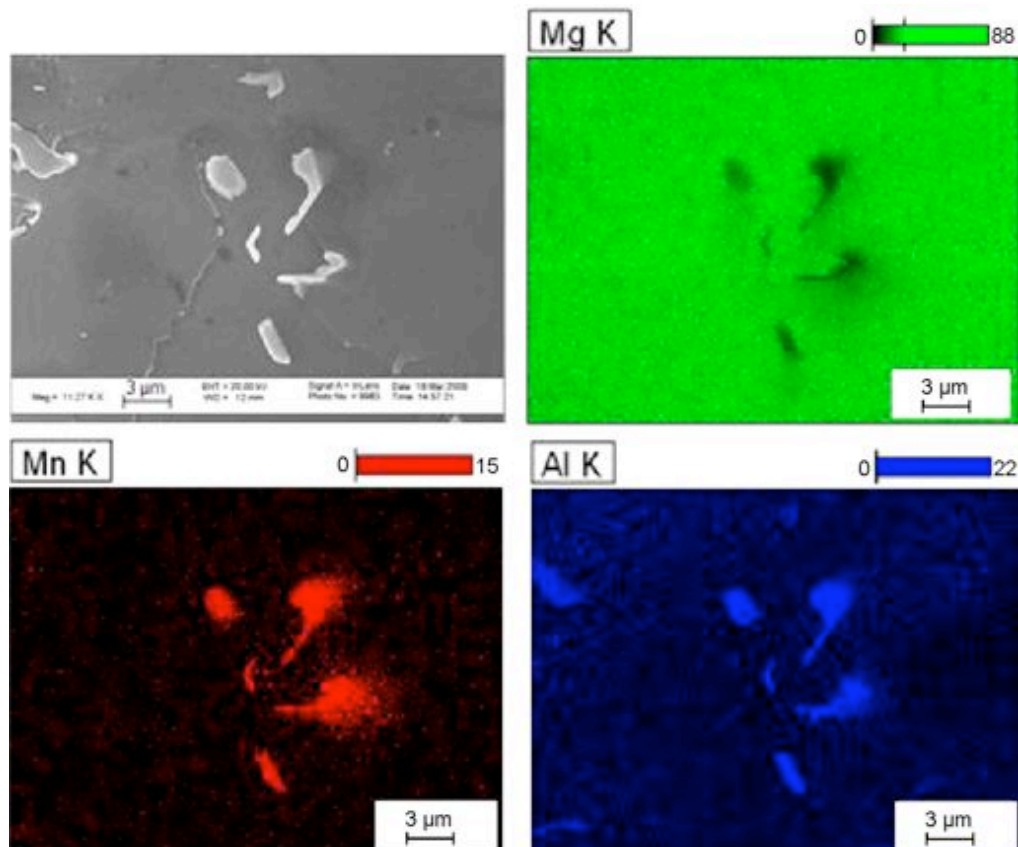
Fig. 5. EDS of AM60B without Al_4C_3 177 °C, accelerating voltage 20.0 kV.
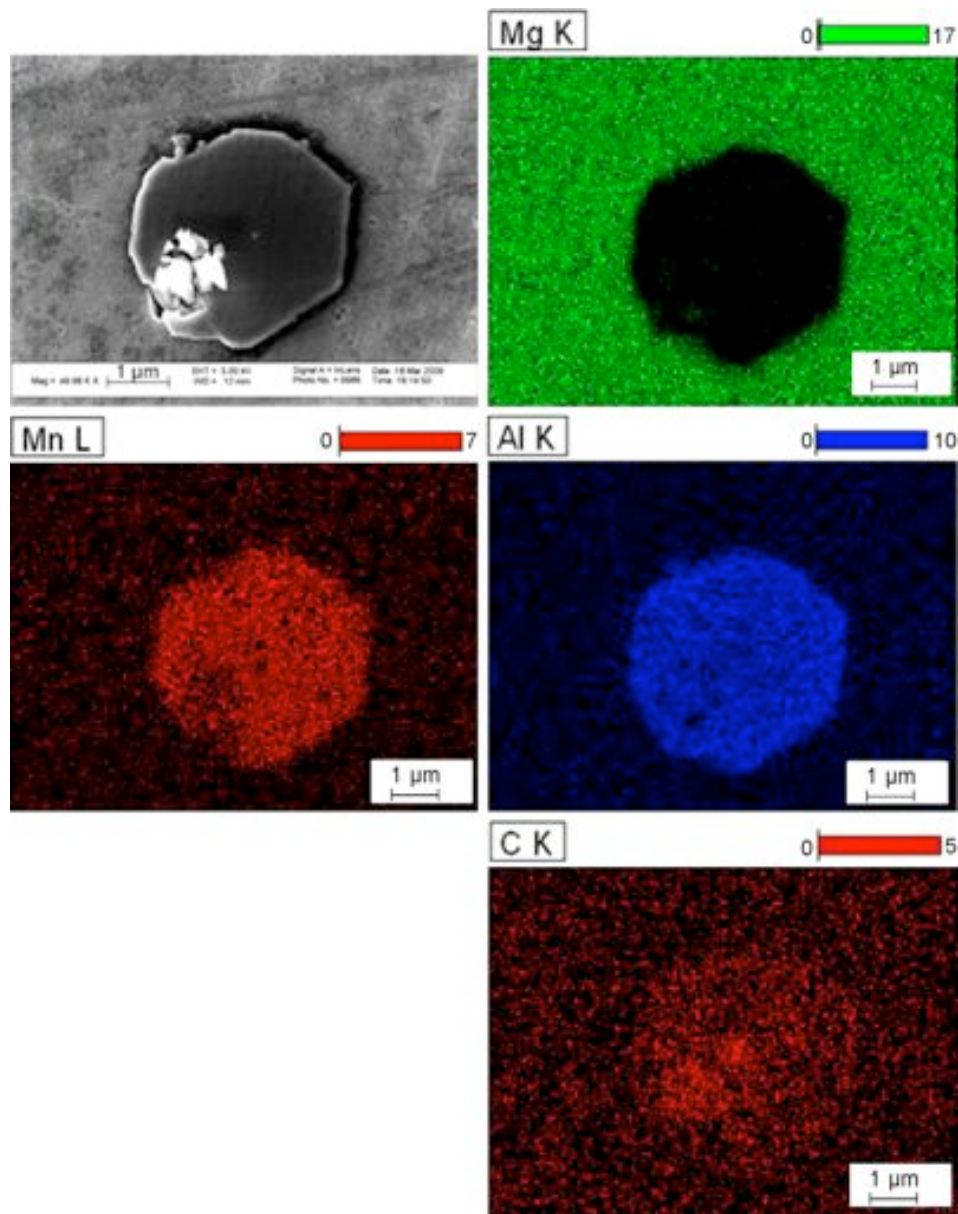
Fig. 6. EDS of AM60B/5%Al$_4$C$_3$ 177 °C, accelerating voltage 5.0 kV, illustrating duplex nucleation: Al$_8$Mn$_5$ nucleated at the surface of an Al$_4$C$_3$ particle all within an α-Mg grain.

phases. Duplex nucleation of Al$_4$C$_3$ is found to have significant effect on grain refinement in Mg–Al alloys containing Mn.

3.6. XRD analysis

Fig. 7a shows the X-ray diffraction pattern of pure AM60B. The spectrum consists of mostly Mg peaks. In addition, low-index MnAl$_6$ peaks and high-index Al$_8$Mn$_5$ peaks were observed at low 2θ values. Also, a few peaks indicating the presence of the beta Mg$_{17}$Al$_{12}$ phase were observed.

Fig. 7b shows the X-ray diffraction pattern of pure AM60B with 5 wt% Al$_4$C$_3$. The spectrum is very similar to the pure AM60B spectrum with the exception of the MnAl$_6$ peaks, which are not observed in the AM60B/5%Al$_4$C$_3$ spectrum. This further supports the theory that the Mn has nucleated in the form of Al$_8$Mn$_5$ due to the addition of Al$_4$C$_3$. Diffraction peaks corresponding to the Al$_4$C$_3$ were not observed in the AM60B/5%Al$_4$C$_3$ spectrum. This could be a result of the Al$_4$C$_3$ being encapsulated by the Al$_8$Mn$_5$ phase and

supports the claim that the surface of Al$_4$C$_3$ acts as a nucleation site for the Al$_8$Mn$_5$ phase.

An XRD sample was also prepared of pure Al$_4$C$_3$ microparticles that were added to the Mg melts confirming crystallographic structure and chemical composition of the microparticles used. Al$_4$C$_3$ particles were placed on a glass slide and sputtered with a thin layer of gold for examination. Fig. 8 shows the XRD spectrum from the Al$_4$C$_3$ particles with Al$_4$C$_3$ reference peaks below displayed below the XRD spectrum.

3.7. EPMA analysis

Electron probe microanalysis (EPMA) analysis was conducted using wavelength dispersive spectroscopy (WDS) to examine the K-α emission spectra of aluminum and carbon at an accelerating voltage of 8 KeV in conjunction with air jet anti-contamination. The sample of Al$_4$C$_3$ microparticles that were used for XRD to confirm crystallographic structure and chemical composition were also
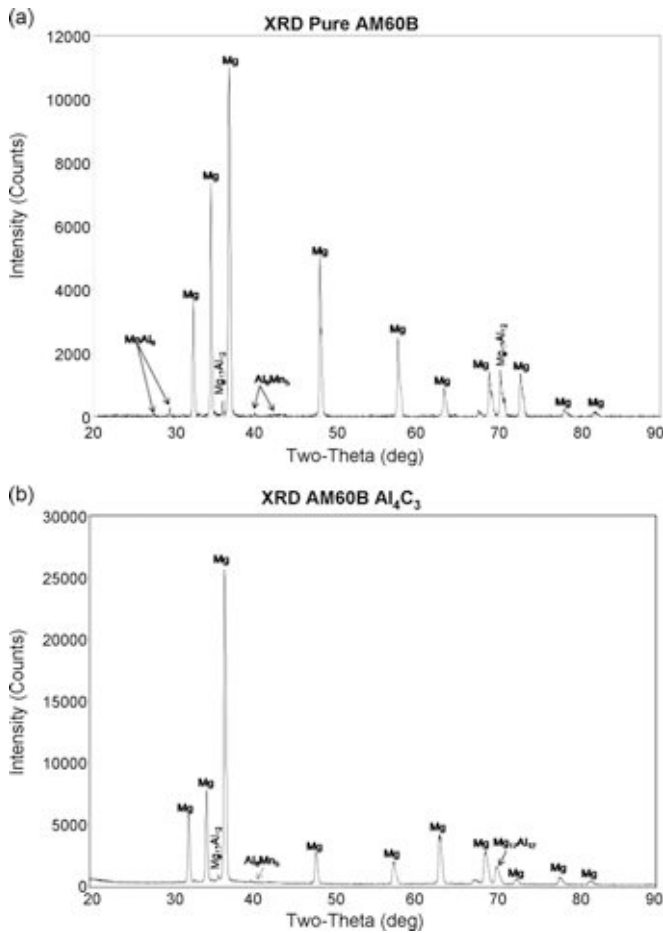
Fig. 7. XRD spectrum of AM60B (a) without and (b) with the addition of 5 wt% Al_4C_3.

used as the standard material for EPMA to determine the distinct emission spectra of aluminum and carbon for the Al_4C_3 microparticles (Fig. 9c and d). Fig. 9c shows the standard Al_4C_3 peak for carbon with a smaller peak located at about 0.263 KeV, which corresponds to a second order oxygen K-α emission. This second order K-α peak for oxygen can be attributed to slight oxidation of the sample from time of preparation to WDS scan. Background spectra were taken for the AM60B/5%Al_4C_3 within the α-Mg grains to attain typical carbon and aluminum wavescan counts for the sam
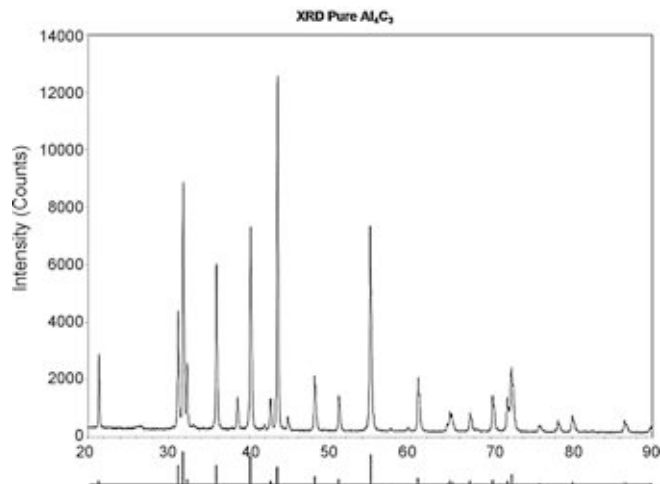
Fig. 8. XRD spectrum of Al_4C_3 with reference peaks displayed below.

ple (Fig. 9a and b). WDS was conducted on the polygonal Al_8Mn_5 phases in AM60B/5%Al_4C_3 to determine if these phases encapsulate Al_4C_3. From Fig. 9a and b it can be seen that the Al_8Mn_5 phases have significantly higher concentrations of carbon and aluminum compared to the background (α-Mg) matrix. The difference in carbon base line height in Fig. 9a is due to the difference between a primarily Mg interaction volume (≈15 wavescan counts) verses an interaction volume comprised of $Al_8Mn_5 + Al_4C_3$ (≈35 wavescan counts). In Fig. 9c and d significant agreement in peak height and location can be seen between the standard Al_4C_3 and the polygonal Al_8Mn_5 phases confirming the presence of carbon and aluminum within Al_8Mn_5.

3.8. Mg/5%Al₄C₃

To evaluate the most commonly accepted theory that carbon inoculation based grain refinement in Mg–Al based alloys occurs when α-Mg nucleates at the surface of aluminum containing carbides, pure Mg and Mg/5 wt%Al_4C_3 were cast to see if there would be any significant grain refinement in a Mn-free environment containing Al_4C_3. Average grain size was measured using the linear intercept method from optical micrographs for pure Mg and Mg/5%Al_4C_3 and is found to be $383 \pm 88\,\mu m$ and $49 \pm 16\,\mu m$, respectively. Fig. 10 shows the significant grain refinement of the Mg/5%Al_4C_3 compared to the pure Mg, and indicates that the surface of Al_4C_3 is an effective nucleation site for α-Mg. Fig. 10b shows an optical micrograph of the dark Al_4C_3 particles intragranular and intergranular in the Mg matrix. The average microhardness for the pure Mg and Mg/5%Al_4C_3 and is 25.3 ± 4.5 HK and 35.9 ± 0.7 HK, respectively. SEM and optical micrographs show intragranular Al_4C_3 microparticles in the Mg matrix and that the Mg melt did not react with the Al_4C_3 to form $Mg_{17}Al_{12}$.

WDS was performed on the particles within the Mg grains examining the carbon and aluminum K-α peaks compared to that of the standard Al_4C_3 particles (Fig. 11). In Fig. 11 significant agreement in peak location and amplitude can be seen between the standard Al_4C_3 and the Al_4C_3 particle in the Mg grain indicating that these particles are Al_4C_3. The addition of Al_4C_3 to Mg leads to dramatic grain refinement $(383 \rightarrow 49\,\mu m)$ supporting the hypothesis that Al_4C_3 can effectively nucleate Mg grains [6–12,14].

3.9. Mg–6%Al/5%Al₄C₃

Evaluation of duplex nucleation $(Al_4C_3 \rightarrow Al_8Mn_5 \rightarrow \alpha\text{-Mg})$ in Mg–Al alloys is further examined by processing Mn-free Mg–6%Al and Mn-free Mg–6%Al/5 wt%Al_4C_3 and inspecting the microstructure for grain refinement. Kim et al. cast Mn-free Mg–9%Al alloy with 0.6% C_2Cl_6 and found it to yield little grain refinement when compared to AZ91. When 0.3% Mn was added to Mg–9%Al alloy with 0.6% C_2Cl_6 significant grain refinement was seen indicating that Mn plays an intricate role in carbon inoculation based grain refinement. SEM investigation of the Mn-free Mg–9%Al alloy with 0.6% C_2Cl_6 found that the Al_4C_3 particles were scarcely observed and of those most Al_4C_3 particles coexisted with the $Mg_{17}Al_{12}$ phase [5].

Average grain size was measured using the linear intercept method from optical micrographs for Mn-free Mg–6%Al and Mn-free Mg–6%Al/5%Al_4C_3 and found to be $33 \pm 6\,\mu m$ and $34 \pm 11\,\mu m$, respectively. The average microhardness for the Mn-free Mg–6%Al and Mn-free Mg–6%Al/5%Al_4C_3 is 53.5 ± 1.5 HK and 49.6 ± 5.2 HK, respectively. Fig. 12 is an optical micrograph of Mn-free Mg–6%Al/5%Al_4C_3 in which the dark Al_4C_3 particles are predominantly intergranular and segregated from the lighter $Mg_{17}Al_{12}$ beta phase. With the addition of 6% Al to the Mg the Al_4C_3 microparticles are found at the grain boundaries of the α-Mg and no grain refinement is achieved. The Al_4C_3 microparticles were completely segregated from the $Mg_{17}Al_{12}$ phase (indicated in Fig. 12).
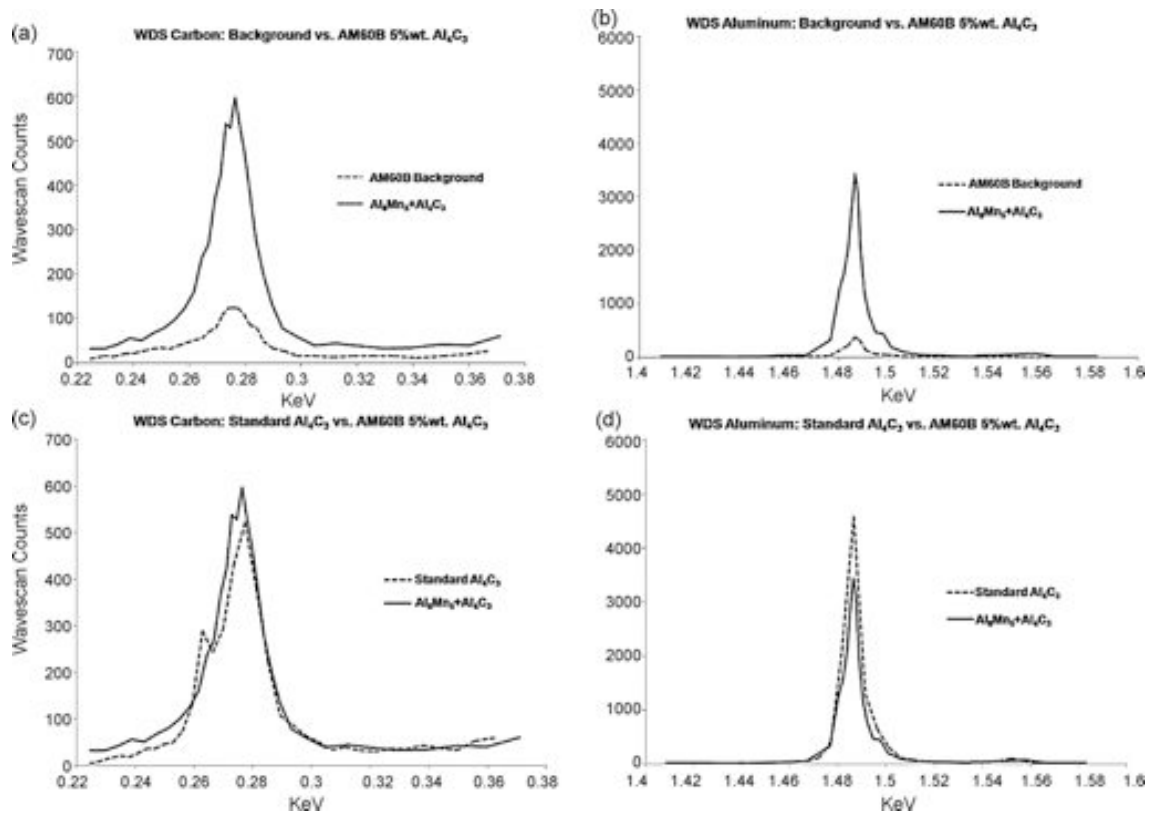
Fig. 9. WDS of Al_8Mn_5 polygonal phases containing Al_4C_3 in AM60B/5%Al_4C_3 (a) vs. α-Mg examining carbon K-α peak, (b) vs. α-Mg examining aluminum K-α peak, (c) vs. standard Al_4C_3 examining carbon K-α peak, and (d) vs. standard Al_4C_3 aluminum K-α peak.
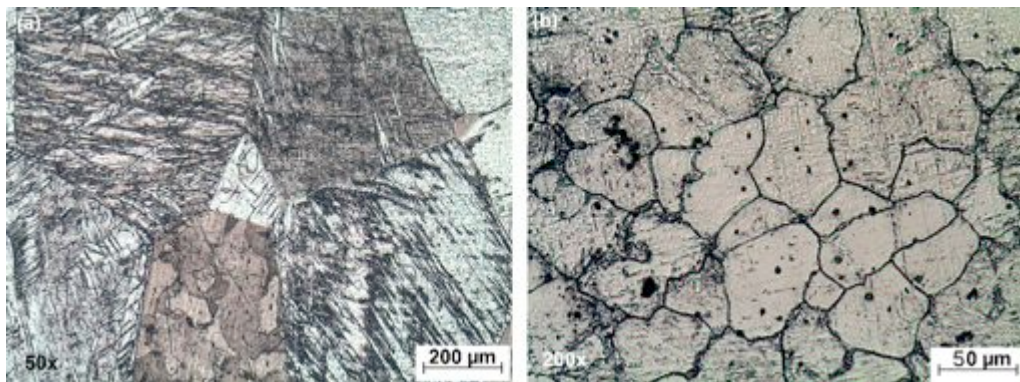
Fig. 10. Optical micrograph of Mg (a) without and (b) with 5 wt% Al_4C_3.
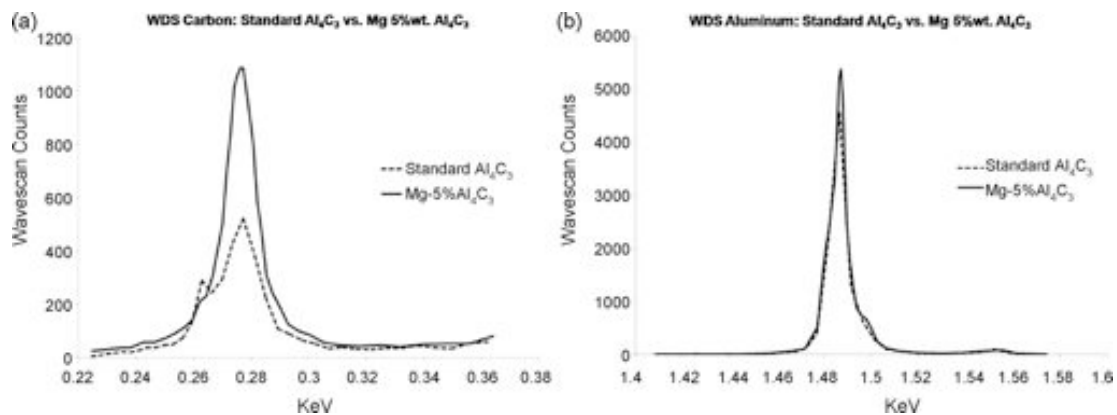
Fig. 11. WDS of Al_4C_3 particles in Mg/5%Al_4C_3 (a) vs. standard Al_4C_3 examining carbon K-α peak and (b) vs. standard Al_4C_3 aluminum K-α peak.
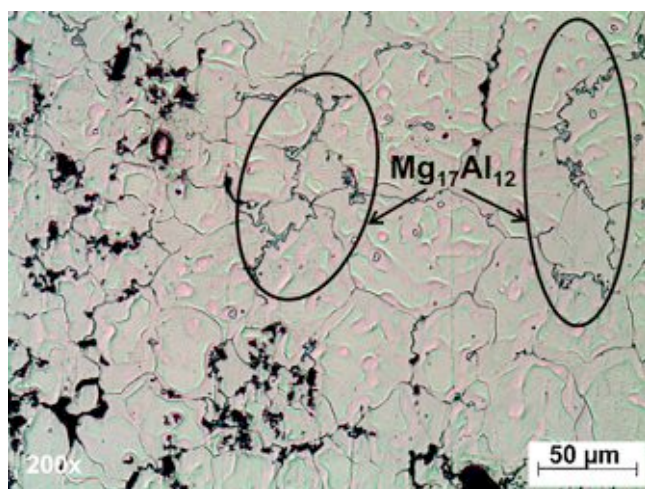
Fig. 12. Optical micrograph of Mn-free Mg–6%Al/5%Al$_4$C$_3$, illustrating the typical segregation of Al$_4$C$_3$ particles (dark) from Mg$_{17}$Al$_{12}$ beta phase (light intergranular regions, indicated).

Lu et al. have shown that the addition of Al$_4$C$_3$ into high purity Mg–3%Al can yield significant grain refinement (400 → 170 μm) [6]; however, Kim et al. found the addition of 0.6% C$_2$Cl$_6$ to Mn-free Mg–9%Al yielded little grain refinement [5]. This suggests that the tendency of the Al$_4$C$_3$ particles to be segregated at the solid–liquid (S–L) interface increases as the percentage of Al increases in high purity Mg–Al alloy systems. There is a few locations of local grain refinement (areas <50 μm) seen in the Mn-free Mg–6%Al/5 wt%Al$_4$C$_3$; however it occurs at regions where Al$_4$C$_3$ has segregated to the grain boundaries. In these locations segregated Al$_4$C$_3$ particles at the solid–liquid interface greatly affect constitutional undercooling and restrict grain growth causing localized refinement. Mn plays an intricate role in the grain refinement capabilities of Al$_4$C$_3$ in Mg–Al alloy systems containing ≥6%Al; however, in Mg–Al alloys with ≤3%Al the addition of Al$_4$C$_3$ is able to nucleate the α-Mg grains and yield significant grain refinement [5,6].

4. Conclusion

Ultrasonic cavitation based dispersion of 5 wt% Al$_4$C$_3$ in AM60B, Mg, and Mn-free Mg–6%Al were investigated with optical microscopy, SEM, EDS, EPMA, and XRD to determine the principal grain refining mechanisms in Mg–Al alloy systems. The two underlying refinement mechanisms with the addition of Al$_4$C$_3$ in AM60B, Mg, and Mn-free Mg–6%Al are: duplex nucleation hypothesis (Al$_4$C$_3$ → Al$_8$Mn$_5$ → α-Mg) and Al$_4$C$_3$ nuclei hypothesis (Al$_4$C$_3$ → α-Mg). The morphology change of Al–Mn phases from irregular to polygonal Al$_8$Mn$_5$ with the addition of 5 wt% Al$_4$C$_3$ in AM60B indicates that Al$_4$C$_3$ acts as a heterogeneous nucleation site for Al$_8$Mn$_5$; which in turn, acts as the nucleation site for α-Mg and further supports the duplex nucleation theory. The addition of 5 wt% Al$_4$C$_3$ to pure Mg yields significant grain refinement (383 → 49 μm) which follows the Al$_4$C$_3$ nuclei hypothesis for α-Mg grains. The addition of 5 wt% Al$_4$C$_3$ to Mn-free Mg–6%Al; however, is not refined at all indicating that Al$_4$C$_3$ can only provide grain refinement in Mg–Al alloys ≤3%Al and Mg–Al alloys containing Mn. The tendency of the Al$_4$C$_3$ particles to be segregated at the solid–liquid (S–L) interface increases as the percentage of Al increases in high purity (Mn-free) Mg–Al alloy systems. Mechanical properties (yield strength, tensile strength, ductility, and microhardness) were enhanced by the addition of Al$_4$C$_3$ to AM60B alloy.

References

[1] G. Cao, H. Konishi, X. Li, Journal of Manufacturing Science and Engineering 130 (3) (2008) 1105–1111.
[2] H. Friedrich, B. Mordike, Magnesium Technology—Metallurgy, Design Data, Applications, Springer-Verlag, 2006, pp. 109–143, 315.
[3] F. Czerwinski, Magnesium Injection Molding, Springer, 2007, pp. 19–41.
[4] G. Cao, H. Choi, H. Konishi, S. Kou, R. Lakes, X. Li, Journal of Material Science 43 (2008) 5521–5526.
[5] Y.M. Kim, C.D. Yim, B.S. You, Scripta Materialia 57 (2007) 691–694.
[6] L. Lu, A.K. Dahle, D.H. StJohn, Scripta Materialia 53 (2005) 517–522.
[7] L. Lu, A.K. Dahle, D.H. StJohn, Scripta Materialia 54 (2006) 2197–2201.
[8] M. Qian, P. Cao, Scripta Materialia 52 (2005) 415–419.
[9] A. Dahle, Y. Lee, M. Nave, P. Schaffer, D. StJohn, Journal of Light Metals 1 (2001) 61–72.
[10] P. Cao, M. Qian, D. StJohn, Scripta Materialia 56 (2007) 633–636.
[11] T. Motegi, Materials Science and Engineering A 413–414 (2005) 408–411.
[12] Y. Tamura, N. Kono, T. Motegi, E. Sato, Journal of Japan Institute of Light Metals 48 (8) (1998) 395–399.
[13] Q. Jin, J. Eom, S. Lim, W. Park, B. You, Scripta Materialia 49 (2003) 1129–1132.
[14] M.X. Zhang, P.M. Kelly, J.A. Ma Qian, Taylor, Acta Materialia 53 (2005) 3261–3270.
[15] M. Avedesian, H. Baker, ASM Specialty Handbook—Magnesium and Magnesium Alloys, ASM International, Metals Park, OH, 1999.